Three-dimensional alignment of asymmetric-top molecules induced by polarization-shaped optimal laser pulses

Masataka Yoshida, Norio Takemoto, and Yukiyoshi Ohtsuki

Phys. Rev. A **98**, 053434 — Published 26 November 2018

DOI: 10.1103/PhysRevA.98.053434

Three-dimensional alignment of asymmetric top molecules induced by polarization-shaped optimal laser pulses

Masataka Yoshida[1], Norio Takemoto[2], and Yukiyoshi Ohtsuki[1]*

[1]Department of Chemistry, Graduate School of Science, Tohoku University

6-3 Aramaki Aza-Aoba, Aoba-ku, Sendai 980-8578, Japan

[2]J.R. Macdonald Laboratory, Kansas State University

Manhattan, Kansas 66506, USA

* Corresponding author: ohtsuki@m.tohoku.ac.jp

Tel/fax: +81-22-795-7720

Abstract

Optimal control simulation is applied to numerically design non-resonant laser pulses that maximize the degrees of three-dimensional (3D) alignment of SO_2 using the lowest-order induced-dipole interaction. In our trials, combinations of more than two mutually orthogonal, linearly polarized subpulses are always obtained as the optimal solutions. Each subpulse in the optimal pulses impulsively excites the rotational wave packet. The optimal pulses effectively cooperate with the rotational dynamics up to only a few partial revival timings owing to the rotational dephasing that determines the effective control periods. The control mechanisms are interpreted in terms of the time derivatives of the expectation values of the squares of the direction cosines, that of the rotational energy, and the interplay between them. We find a special and important role of the last subpulses as they align the molecular axes using the interaction through the two smallest polarizability components, while the other subpulses excite the rotational wave packet mainly through the largest polarizability component. The control pulses composed of the specified number of subpulses are also numerically optimized by actively utilizing the instantaneous penalty to systematically show the superiority of the use of more than two subpulses over that of two subpulses, the latter of which leads to the saturation of the degree of 3D alignment as a function of total fluence.

I. Introduction

Molecular alignment is a fundamental technique that enables us to observe and manipulate molecular wave functions in a molecule-fixed frame [1, 2]. A short non-resonant laser pulse, the temporal width of which is much shorter than a typical rotational period, is often used to align molecules because the non-resonant pulse can impose a controlled strong electric field, i.e., a torque on the molecules at the right timing through induced-dipole interaction [3]. The rotational wave packet reaches highly aligned states (revivals [4]) after the excitation, i.e., in the field-free condition [5-7].

Some studies have proposed control schemes to three-dimensionally align asymmetric top molecules in the field-free condition [10-16]. For example, a combination of two mutually orthogonal, linearly polarized laser pulses was numerically studied [8], the effectiveness of which was experimentally demonstrated by using SO_2 at the rotational temperature of ~10 K [9]. In the so-called hold-and-spin scheme [10, 11], a combination of linearly polarized laser pulses is also used in which the first laser with a long temporal width holds the most polarizable molecular axis instead of impulsively exciting it. The modified version, called a truncated hold-and-spin scheme, turns off the first pulse rapidly, realizing field-free 3D alignment [11]. A numerical study that used a pair of orthogonal Gaussian pulses with six optimized pulse parameters indicated that the pulse has a general form consisting of overlapping pulses with slightly displaced temporal positions [12]. The numerical study would confirm the effectiveness of the hold-and-spin scheme. A long elliptically polarized laser pulse with rapid truncation [13] and a single short elliptically polarized laser pulse with "optimal" ellipticity [14] were also studied. In another numerical study [15] that used multiple elliptically polarized laser pulses with the same ellipticity, significant improvement of the degree of 3D alignment of SO_2 was not observed. On the other hand, a recent study reported the effectiveness of multiple

elliptically polarized laser pulses with different ellipticities as well as a linearly polarized laser pulse in combination with a sequence of elliptically polarized laser pulses [16].

As explained above, uncertainty remains regarding how to best align asymmetric molecules three-dimensionally. In particular, the superiority of using the control pulse that is composed of more than two subpulses [16] has not been fully understood. This situation justifies the present optimal control study in which we fully optimize a laser pulse including its time-dependent polarization vectors to best achieve the 3D alignment [7, 17, 18]. Here, we consider a rigid body model of SO_2 as it is often used to evaluate the effectiveness of control schemes [9, 15]. The present simulation will demonstrate the advantage of the combination of more than two linearly polarized subpulses. We briefly summarize the numerical procedures in Sec. II. The results and the optimal control mechanisms are discussed in Sec. III. In Sec. IV, we summarize the present study.

II. Theory: Optimal control simulation

We consider an asymmetric top molecule that interacts with a non-resonant laser pulse, $\boldsymbol{E}(t)$, through the lowest-order induced dipole, i.e., the polarizability, $\vec{\vec{\alpha}}$. As shown in Fig. 1, we introduce a space-fixed frame and a molecule-fixed frame, which are defined by sets of unit vectors, $\{\mathbf{e}_X, \mathbf{e}_Y, \mathbf{e}_Z\}$ and $\{\mathbf{e}_a, \mathbf{e}_b, \mathbf{e}_c\}$, respectively. The Hamiltonian is given by

$$H(t) = H_0 + V(t) = AJ_a^2 + BJ_b^2 + CJ_c^2 - \frac{1}{2}\vec{\vec{\alpha}}\boldsymbol{E}(t)\boldsymbol{E}(t), \qquad (1)$$

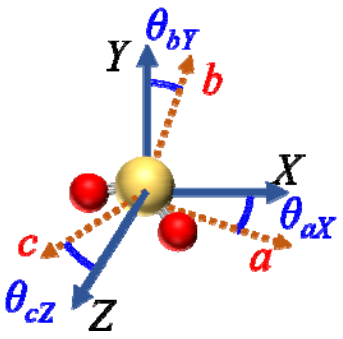

Figure 1

Molecule-fixed *a*-, *b*-, and *c*-axes of SO_2 and space-fixed *X*-, *Y*-, and *Z*-axes. Three of the angles between the molecule-fixed axes and the space-fixed axes are shown.

where A (J_a), B (J_b), and C (J_c) are rotational constants (components of the angular momentum operator, $\boldsymbol{J}$) associated with the molecule-fixed frame. The eigenstate of H_0 is expressed as the linear combination of the eigenstates of a symmetric top, $\{|JKM\rangle\}$, such that $|J\tau M\rangle = \sum_K a_{\tau K}^J |JKM\rangle$, where J, K, and M are the quantum numbers of $\boldsymbol{J}^2$, J_c, and J_Z (the space-fixed Z component of $\boldsymbol{J}$), respectively [1]. Because of the C_{2v} symmetry of SO_2 and the nuclear spin statistics, only even-numbered K 's are allowed. We assume that the laser pulse is expressed as the sum of the *X* and *Y* components

$$\boldsymbol{E}(t) = E_X(t)\mathbf{e}_X + E_Y(t)\mathbf{e}_Y . \qquad (2)$$

The optimized *X* and *Y* components, $E_X(t)$ and $E_Y(t)$, automatically lead to the optimized time-dependent polarization condition. The time evolution of the density operator, $\rho(t)$, is described by the Liouville equation:

$$i\hbar\frac{\partial}{\partial t}\rho(t)=[H(t),\rho(t)], \tag{3}$$

where the initial condition is given by the Boltzmann distribution. Here, we neglect decoherence effects by assuming low gas pressure.

In optimal control simulation, we specify our control objective by using the target Hermitian operator, W [19]. Here, we summarize the procedure without explicitly specifying W. We numerically design an optimal pulse that maximizes the objective functional, $F=\mathrm{Tr}\{W\rho(t_\mathrm{f})\}$, i.e., the target expectation value at the specified final time, t_f [20]. Although a pulse with quite high intensity may lead to a large target expectation value, it may also induce undesirable side effects. To avoid this, we replace $\vec{\alpha}$ with $\vec{\alpha}_\gamma\equiv\vec{\alpha}[1+i\gamma(t)]$, where the positive function, $\gamma(t)$, will be referred to as an instantaneous penalty function [21, 22]. Because the $\gamma(t)$-dependent non-Hermitian part, which is proportional to the pulse intensity, introduces the penalty due to the reduction in the norm, a suitable choice of the function, $\gamma(t)$, can lead to an optimal pulse with reasonably high intensity. Note that after obtaining the optimal pulses, we recalculate all the physical properties using the original equation of motion without $\gamma(t)$, i.e., Eq. (3).

By applying calculus of variations to the objective functional, we derive the coupled pulse-design equations, which are composed of

$$\mathrm{Im}\,\mathrm{Tr}\{\xi_\gamma(t)\vec{\alpha}_\gamma\boldsymbol{E}(t)\rho_\gamma(t)\}=0, \tag{4}$$

$$i\hbar\frac{\partial}{\partial t}\rho_\gamma(t)=[H_\gamma(t),\rho_\gamma(t)], \tag{5}$$

and

$$i\hbar\frac{\partial}{\partial t}\xi_\gamma(t)=[H_\gamma^\dagger(t),\xi(t)], \tag{6}$$

where $\xi_\gamma(t)$ is the Lagrange multiplier that represents the constraint due to Eq. (5). In Eqs. (4)–(6), the suffix, γ, is introduced to explicitly indicate that we have introduced the instantaneous penalty function. As shown above, the density operator formalism is convenient to formally derive the pulse-design equations. In numerical simulation, however, we expand the density operator and the Lagrange multiplier in terms of a set of wave functions and iteratively solve the pulse-design equations in the wave-function form to reduce computational costs.

Finally, we summarize the parameters used in the simulation in Sec. III. We adopt the rotational constants, $A=2.03\ \mathrm{cm}^{-1}$, $B=0.344\ \mathrm{cm}^{-1}$, and $C=0.294\ \mathrm{cm}^{-1}$, and the polarizability components, $\alpha_{aa}=31.3\ \text{Å}^3$, $\alpha_{bb}=20.8\ \text{Å}^3$, and $\alpha_{cc}=18.7\ \text{Å}^3$, which are taken from Refs. [23] and [24], respectively. Temperature is set to 1.0 K. All times are measured in units of "rotational period", $T_{\mathrm{rot}}=1/2(B+C)=26.2\ \mathrm{ps}$. We numerically integrate the equations by using the 5$^{\mathrm{th}}$-order Runge-Kutta method with the temporal grid, 10^{-5} (units of T_{rot}), and iteratively solve the coupled pulse-design equations by using the monotonically convergent

algorithm [17, 18, 21]. We assume a circularly polarized laser pulse as the initial guess field, that is,

$$E_X^{(0)}(t) = \varepsilon^{(0)}(t)\cos\omega t \quad \text{and} \quad E_Y^{(0)}(t) = \varepsilon^{(0)}(t)\sin\omega t\,, \tag{7}$$

where the wavelength of the optical frequency is set to 1600 nm for convenience. We use the initial envelope function with a rather flat structure, $\varepsilon^{(0)}(t)$, given by

$$\varepsilon^{(0)}(t) = \begin{cases} \varepsilon_0 \sin(\dfrac{t}{2\tau_L}\pi) & 0 \le t < \tau_L \\ \varepsilon_0 & \tau_L \le t \le t_{\mathrm{f}} - \tau_L \\ \varepsilon_0 \sin(\dfrac{t_{\mathrm{f}} - t}{2\tau_L}\pi) & t_{\mathrm{f}} - \tau_L < t \le t_{\mathrm{f}} \end{cases} \tag{8}$$

with $\tau_L = 0.1\,T_{\mathrm{rot}}$. The value of ε_0, which is empirically determined, is in the order of 0.1 GV/m.

III. Results and Discussion

We first optimize the laser pulses by assuming a slightly long final time, $t_{\mathrm{f}} = 4.0$. This is because we do not know how much the optimized laser pulses can cooperate with the imperfect alignment revivals in the presence of strong rotational dephasing due to the lack of a regular energy-level structure. To specify the target operator, we choose two of the three molecular axes to be aligned along the polarization vectors of the laser pulse. For example, when the *a* and *b* molecular axes are chosen as the target axes, we adopt the target operator,

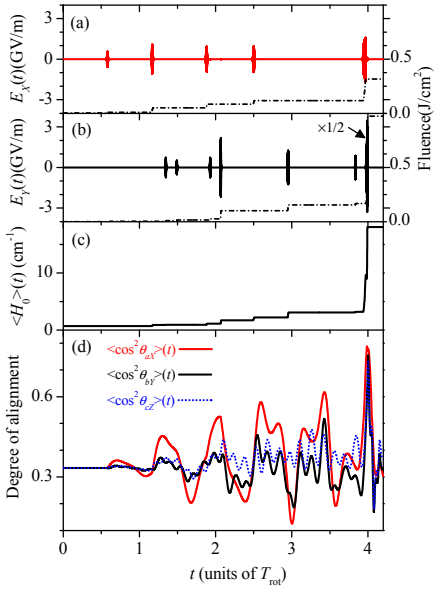

Figure 2

Results of optimization control simulation with the final time, $t_f = 4.0$, in units of T_{rot} when the *a*- and *b*-axes are chosen as the target axes. Optimized (a) *X* and (b) *Y* components of the laser field. Dot-dashed lines indicate fluence as a function of time. (c) Expectation value of the free rotational Hamiltonian, H_0. (d) Red solid, black solid, and blue dashed lines represent the time evolution of the degrees of alignment, $\left\langle \cos^2 \theta_{aX} \right\rangle (t)$, $\left\langle \cos^2 \theta_{bY} \right\rangle (t)$, and $\left\langle \cos^2 \theta_{cZ} \right\rangle (t)$, respectively.

$$W = \frac{1}{3}\left[(\mathbf{e}_a \cdot \mathbf{e}_X)^2 + (\mathbf{e}_b \cdot \mathbf{e}_Y)^2 + (\mathbf{e}_c \cdot \mathbf{e}_Z)^2 \right] = \frac{1}{3}\left(\cos^2 \theta_{aX} + \cos^2 \theta_{bY} + \cos^2 \theta_{cZ} \right). \quad (9)$$

This is the sum of the square of the direction cosines, the expectation value of which will be referred to as the averaged degree of alignment. The results of the optimal control simulation are shown in Fig. 2. We see from Figs. 2(a) and (b) that the optimal laser pulse is composed of mutually orthogonal, linearly polarized subpulses. The pulse fluence as a function of time indicates that the subpulses appearing in the second half could dominate the control. This

suggests that a shorter control time, e.g., $t_f = 2.0$, would be sufficient for the optimal pulse to achieve a high degree of 3D alignment (see Fig. 3). Figure 2(c) shows that each subpulse in the optimal pulse monotonically increases the rotational energy although the last *Y* subpulse introduces a small dip. This monotonic increase in rotational energy is quite reasonable because higher rotational excitation is necessary to achieve a higher degree of 3D alignment. In fact, this point will provide one of the bases to discuss the control mechanisms later. Figure 2(d) shows the time-dependent expectation values of the direction cosines in Eq. (9). Their oscillation amplitudes gradually increase and reach maximum values immediately after the significant enhancement by the last *X* and *Y* subpulses.

Table I: Optimized degrees of alignment for three sets of the target molecular axes. The target axes, (*a*, *b*), for example, mean that the *a* and *b* molecular axes should be aligned along the polarization vectors of the laser pulse. The angle, θ_a, denotes the angle between the *a*-axis and one of the space-fixed axes along which the *a*-axis mostly aligns. The space-fixed axes are denoted in the parentheses. The angles, θ_b and θ_c, are defined similarly.

target axes	(*a*, *b*)	(*b*, *c*)	(*c*, *a*)	(*a*, *b*, *c*)[1)]
averaged degree of alignment	0.75	0.71	0.73	0.77
$\left\langle \cos^2 \theta_a \right\rangle$	0.78 (*X*)	0.72 (*Z*)	0.79 (*X*)	0.79 (*X*)
$\left\langle \cos^2 \theta_b \right\rangle$	0.75 (*Y*)	0.71 (*X*)	0.71 (*Z*)	0.77 (*Y*)
$\left\langle \cos^2 \theta_c \right\rangle$	0.73 (*Z*)	0.72 (*Y*)	0.70 (*Y*)	0.77 (*Z*)
pulse fluence (J cm^{-2})	1.3	1.5	1.0	1.4

1) For reference, we show the optimized degrees of alignment when the non-resonant laser pulse is assumed to be composed of linearly polarized, *X*-, *Y*- and *Z*-components.

The degrees of alignment realized by the optimal pulses are summarized in Table I, in which all the three cases of the target molecular axes are considered. We see from Table I that reasonably high degrees of alignment are achieved independent of the choice of the target axes. Although we do not show the numerical results except for those in Fig. 2, the optimal pulses are always composed of mutually orthogonal, linearly polarized subpulses. We have not found elliptically polarized subpulses in the optimal pulses in our trials. For reference, we also optimize the elliptically polarized laser pulse with a fixed ellipticity of 0.55, and that with 0.78 (not shown). They lead to the averaged degrees of alignment of 0.62 and 0.63, respectively, when the *a*-axis (*c*-axis) is aligned along the *X*-axis (*Y*-axis). As these values are considerably smaller than those given in Table I, the combination of elliptically polarized subpulses with a fixed ellipticity cannot be an optimal control approach, consistent with the conclusion in Ref. [15]. In addition, we also optimize a combination of linearly polarized *X*-, *Y*- and *Z*-pulses simultaneously. As expected, the excitation from the three mutually orthogonal directions leads to the largest degree of alignment, as shown in Table I. However, we will not further discuss this control scheme because it would require much more complex experimental arrangements than the combination of *X*- and *Y*-pulses.

In Fig. 3, we optimize the laser pulse by assuming a control time that is half that in Fig. 2, i.e., $t_f = 2.0$. We choose the *a*- and *b*-axes as the target axes because this combination led to the optimal pulse with the simplest temporal structure. The optimized *X*- and *Y*-pulses in Figs. 3(a) and (b) have quite similar structures to those in the second half in Figs. 2(a) and (b), respectively. The averaged degree of alignment, 0.75, in Fig. 3 is the same as that in Fig. 2 to two significant figures although the value of each component is slightly different. We see a total of five subpulses in Fig. 3, which almost monotonically increase the rotational energy, as shown in Fig. 3(c). Figure 3(d) shows the expectation values of the squares of the direction

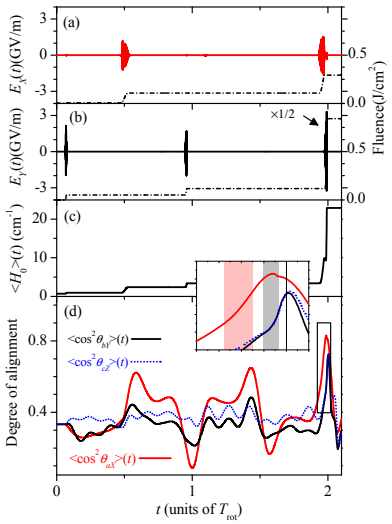

Figure 3

Results of optimization control simulation with the final time, $t_f = 2.0$, in units of T_{rot} when the *a*- and *b*-axes are chosen as the target axes. Optimized (a) *X* and (b) *Y* components of the laser field. Dot-dashed lines indicate fluence as a function of time. (b) Expectation value of the free rotational Hamiltonian, H_0. (c) Red solid, black solid, and blue dashed lines represent the time evolution of the degrees of alignment, $\left\langle \cos^2 \theta_{aX} \right\rangle (t)$, $\left\langle \cos^2 \theta_{bY} \right\rangle (t)$, and $\left\langle \cos^2 \theta_{cZ} \right\rangle (t)$, respectively. Inset shows a magnified view of the degrees of alignment around the final time indicated by a solid vertical line. The red (gray) color-coded bar shows the temporal region in which the absolute value of the amplitude of the *X* (*Y*) subpulse is greater than 1 GV/m.

cosines as a function of time, from which we see that their amplitudes are significantly enhanced around the final time. The inset offers a magnified view of the region framed by a rectangle in Fig. 3(d).

As our control objective is specified by the expectation value of the target operator [Eq. (9)] at the final time, $\langle W \rangle (t_f)$, we rewrite it as

$$\langle W \rangle (t_{\mathrm{f}}) = \int_0^{t_{\mathrm{f}}} dt \frac{d}{dt} \langle W \rangle (t) + \langle W \rangle (0) . \tag{10}$$

We thus focus on the time-dependent behavior of the time derivatives of the expectation values of the squares of the direction cosines to examine the role of each subpulse during the control period. We first discuss the role of the last *Y* subpulse, which contributes to 64% of the total fluence. We see from the inset in Fig. 3 that the last *Y* subpulse significantly increases $\left\langle \cos^2 \theta_{bY} \right\rangle (t)$ and $\left\langle \cos^2 \theta_{cZ} \right\rangle (t)$ almost by the same amount. This behavior predicted by the optimal control simulation means that their time derivatives should be almost the same at that timing, i.e.,

$$\frac{d}{dt} \left\langle \cos^2 \theta_{bY} \right\rangle (t) \simeq \frac{d}{dt} \left\langle \cos^2 \theta_{cZ} \right\rangle (t) . \tag{11}$$

We now try to find the conditions for deriving Eq. (11). If we assume that the last *Y* subpulse appears when $\left\langle \cos^2 \theta_{aY} \right\rangle (t)$ and $\left\langle \cos^2 \theta_{cX} \right\rangle (t)$ take extreme values, i.e., $d \left\langle \cos^2 \theta_{aY} \right\rangle (t) / dt = 0$ and $d \left\langle \cos^2 \theta_{cX} \right\rangle (t) / dt = 0$, it will be easy to see that Eq. (11) can be derived by using the normalization conditions, $\mathbf{e}_Y \cdot \mathbf{e}_Y = \mathbf{e}_c \cdot \mathbf{e}_c = 1$. From the inset in Fig. 3, we also see only a slight decrease in $\left\langle \cos^2 \theta_{aX} \right\rangle (t)$, indicating $d \left\langle \cos^2 \theta_{aX} \right\rangle (t) / dt \simeq 0$ at the timing of the last *Y* subpulse. In the end, the last *Y* subpulse can be characterized by the three extreme conditions,

$$\frac{d}{dt} \left\langle \cos^2 \theta_{aX} \right\rangle (t) = 0 , \ \frac{d}{dt} \left\langle \cos^2 \theta_{aY} \right\rangle (t) = 0 , \text{ and } \frac{d}{dt} \left\langle \cos^2 \theta_{cX} \right\rangle (t) = 0 . \tag{12}$$

The first two extreme conditions mean that the undesirable torque imposed on the *a*-axis by the last *Y* subpulse should be minimized because the *a*-axis should be aligned along the *X*-axis at the final time, i.e., immediately after the last *Y* subpulse. The minimization of the undesirable torque is realized not only by maximizing $\left\langle \cos^2 \theta_{aX} \right\rangle(t)$ but also by actively minimizing $\left\langle \cos^2 \theta_{aY} \right\rangle(t)$. The latter condition is quite reasonable because the actual maximum value of $\left\langle \cos^2 \theta_{aX} \right\rangle(t)$ is usually much smaller than the ideal value of 1. We would like to emphasize that the minimization of $\left\langle \cos^2 \theta_{aY} \right\rangle(t)$ can be realized only when the alignment control pulse is composed of more than two subpulses [8]. The remaining extreme condition, $d\left\langle \cos^2 \theta_{cX} \right\rangle(t)\Big/dt = 0$, which means the minimization of $\left\langle \cos^2 \theta_{cX} \right\rangle(t)$, requires that the *c*-axis be on the *YZ*-plane as much as possible. All the three extreme conditions in Eq. (12) cooperate to simultaneously align the *b*- and *c*-axes, as shown in Eq. (11).

To directly connect the above-mentioned alignment control to the rotational excitation, we consider the time derivative of the expectation value of H_0 and obtain the relation [25]

$$\begin{aligned}\frac{d}{dt}\left\langle H_0 \right\rangle(t) = \frac{[E_X(t)]^2}{2}\left\{(\alpha_{aa}-\alpha_{cc})\frac{d}{dt}\left\langle \cos^2 \theta_{aX} \right\rangle(t) + (\alpha_{bb}-\alpha_{cc})\frac{d}{dt}\left\langle \cos^2 \theta_{bX} \right\rangle(t)\right\} \\ + \frac{[E_Y(t)]^2}{2}\left\{(\alpha_{aa}-\alpha_{cc})\frac{d}{dt}\left\langle \cos^2 \theta_{aY} \right\rangle(t) + (\alpha_{bb}-\alpha_{cc})\frac{d}{dt}\left\langle \cos^2 \theta_{bY} \right\rangle(t)\right\}.\end{aligned} \tag{13}$$

If we substitute one of the extreme conditions in Eq. (12) into Eq. (13), we have

$$\frac{d}{dt}\langle H_0\rangle(t) \simeq \frac{[E_Y(t)]^2}{2}(\alpha_{bb}-\alpha_{cc})\frac{d}{dt}\left\langle \cos^2\theta_{bY}\right\rangle(t)\,. \tag{14}$$

In fact, we see from the inset in Fig. 3 that the time derivative, $d\left\langle \cos^2\theta_{bY}\right\rangle(t)/dt$, has a large positive value during the excitation by the last *Y* subpulse. Because of the rather small value of $\alpha_{bb}-\alpha_{cc}$ in Eq. (14), the last *Y* subpulse must supply a large amount of energy to induce the large rotational excitation to highly align the *b*- and *c*-axes along the *Y*- and *Z*-axes, respectively. This explains the large fluence of the last *Y* subpulse.

We next discuss the role of the last *X* subpulse, which appears immediately before the last *Y* subpulse. During the period of *X* subpulse irradiation, Eq. (13) is reduced to

$$\frac{d}{dt}\langle H_0\rangle(t) = \frac{[E_X(t)]^2}{2}\left\{(\alpha_{aa}-\alpha_{cc})\frac{d}{dt}\left\langle \cos^2\theta_{aX}\right\rangle(t)+(\alpha_{bb}-\alpha_{cc})\frac{d}{dt}\left\langle \cos^2\theta_{bX}\right\rangle(t)\right\}. \tag{15}$$

Because $\alpha_{aa}-\alpha_{cc} >> \alpha_{bb}-\alpha_{cc}$ and $d\left\langle \cos^2\theta_{aX}\right\rangle(t)/dt$ has a large positive value during this period (see the inset in Fig. 3), we may say from Eq. (15) that the last *X* subpulse appears when it can efficiently excite the rotational states. Similarly, we can attribute the timings of the other *X* and *Y* subpulses to the favorable timings for the rotational excitation.

We may thus summarize the control mechanism in Fig. 3 as follows. Starting from the initial excitation by the *Y* subpulse, the timing of which would be inversely determined by the specified final time, the rotational wave packet is gradually and effectively excited by the *X* and *Y* subpulses. They cooperate with the motion of the rotational wave packet through the large polarizability differences, $\alpha_{aa}-\alpha_{bb}$ and $\alpha_{aa}-\alpha_{cc}$ [Eq. (13)]. The excitation and the

free propagation adjust the shape of the rotational wave packet to approximately satisfy the three extreme conditions in Eq. (12) immediately before the final time. At this timing, because of these extreme conditions [Eq. (12)], the last *Y* subpulse with a large fluence effectively aligns the *b*- and *c*-axes along the *Y*- and *Z*-axes, respectively, while leaving the *a*-axis almost unchanged so that the *a*-axis keeps aligning along the *X*-axis.

In the above discussion, we have not assumed a specific temporal structure for each subpulse. As confirmed later in Fig. 5, we can replace the subpulses in the optimal pulse with simple Gaussian subpulses without reducing the degree of 3D alignment, provided that the Gaussian subpulses induce impulsive excitation. In addition, we have emphasized the important and special role of the last *Y* subpulse. All the other subpulses are expected to efficiently excite the rotational wave packet by utilizing the largest polarizability component, α_{aa}, to help the last *Y* subpulse align the two minor *b*- and *c*-axes. It would, thus, be natural to ask how many subpulses we can remove while keeping high degrees of alignment. The answer to this question will illustrate the effectiveness of the use of more than two subpulses in the 3D alignment control.

We consider a minimal control pulse to achieve the 3D alignment, which consists of a pair of linearly polarized *X* and *Y* subpulses. The control scheme that utilizes the minimal control pulse will be referred to as a double-pulse control scheme [8]. We assume a pair of Gaussian *X* and *Y* subpulses with specified total pulse fluence and calculate the degrees of alignment as a function of delay time and fluence ratio. Here, we consider the delay time between the two subpulses in the range of $[0, 2.0]$, and the fluence ratio, in the range of $[0, 1.0]$. The values of the ratio, 0 and 1, correspond to the single-pulse excitation. All the Gaussian subpulses considered in the following are assumed to have a fixed temporal width (FWHM), $\sigma = 100$ fs, which is estimated from the last *Y* subpulse in Fig. 3(b). Note that we

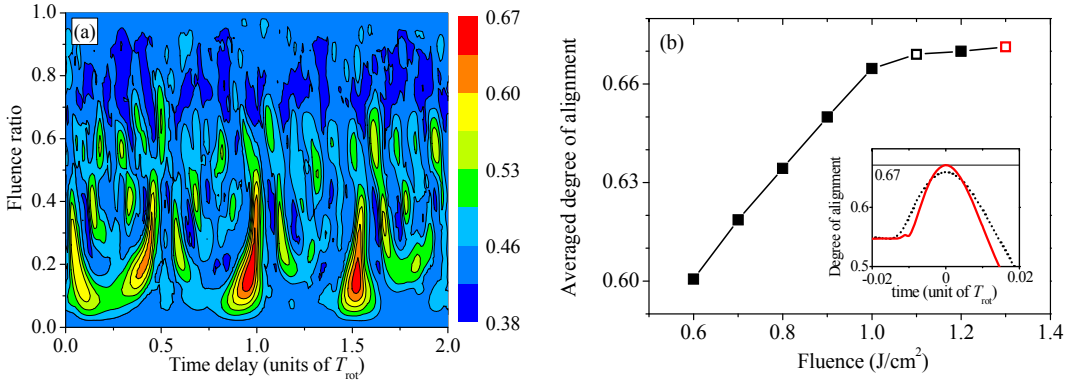

Figure 4

(a) Contour plot of the largest averaged degrees of alignment achieved by mutually orthogonal, linearly polarized Gaussian subpulses (see text) as a function of delay time (horizontal axis) and fluence ratio (vertical axis). As we consider all possible combinations of the target molecular axes with respect to the space-fixed axes, the *X* subpulse is assumed to appear before the *Y* subpulse. Fluence ratio is defined by the *X*-subpulse fluence divided by the total fluence. (b) Maximum averaged degree of alignment as a function of total fluence. The values when the total fluence is 1.1 J/cm^2 and 1.3 J/cm^2 are specified by black and red open squares, respectively. Red solid and black dashed lines in the inset, respectively, show a magnified view of the time evolution of the averaged degrees of alignment when the total fluence is 1.1 J/cm^2 and 1.3 J/cm^2. Each time when each averaged degree of alignment becomes a maximum is set to zero for illustrative purposes.

have numerically checked that the results are robust to the value of σ as long as the so-called impulsive-excitation condition is satisfied. As we consider all possible combinations of the target molecular axes with respect to the space-fixed axes, we assume that the *X* subpulse appears before the *Y* subpulse. For a given set of delay time and fluence ratio, we search the largest value of the averaged degree of alignment until 4.0 after the second (*Y*) subpulse.

Figure 4(a) shows a contour plot that summarizes the results when the total pulse fluence is set to 1.3 J/cm^2. When the largest averaged degree of alignment has a reasonably large value for the given set of the time delay and fluence ratio, we always see that the *a*- and

b-axes are aligned along the polarization vectors. The optimal point, i.e., the point associated with the maximum value in Fig. 4(a) is localized at the delay time of 0.98 and the fluence ratio of 0.20, the latter of which means that the second subpulse has a much larger fluence than the first subpulse. This trend is the same as what we saw in the optimal control simulations (Figs. 2 and 3). However, the maximum value of 0.67 in Fig. 4(a) is considerably smaller than 0.75 given in Fig. 3 even though the total fluence of 1.3 J/cm^2 in Fig. 4(a) is slightly larger than 1.1 J/cm^2 in Fig. 3. We obtain the same figures as those in Fig. 4(a) but with the other total fluence to find the maximum averaged degrees of alignment under the given total fluence (not shown here). Figure 4(b) shows the maximum averaged degrees of alignment as a function of total fluence. We see from Fig. 4(b) that saturation starts around 1.0 J/cm^2. This clearly demonstrates the limitation of the double-pulse control scheme [8] and therefore, justifies the introduction of more than two subpulses to better achieve the 3D alignment.

We now consider an excitation scheme that utilizes more than two subpulses. Figure 5(a) shows five Gaussian subpulses that mimic the subpulses in the optimal pulse in Fig. 3. Each Gaussian subpulse has the same fluence as its counterpart. The inset in Fig. 5(a) is a magnified view of the averaged degree of alignment around the final time. The inset shows that the set of five Gaussian subpulses, which will be referred to as the quintuple-pulse control scheme, reproduces the optimal value of 0.75 in Fig. 3. This confirms that each subpulse in the optimal pulse can be replaced with a simple subpulse, which impulsively excites the rotational wave packet.

Here, we briefly discuss the temperature effects on the effectiveness of the multi-pulse control scheme through a case study. We consider the optimal pulses in Fig. 4(b) (the double-pulse control, 1.3 J/cm^2) and Fig. 5(a) (the quintuple-pulse control, 1.1 J/cm^2). For the sake of semi-quantitative evaluation, we introduce the degree of superiority at temperature, *T*,

which is defined by $s(T)=[<W(T)>_{\max}^{(5)}-1/3]/[<W(T)>_{\max}^{(2)}-1/3]$. Here, $<W(T)>_{\max}^{(5)}$ ($<W(T)>_{\max}^{(2)}$) is the maximum averaged degree of alignment achieved by the quintuple-pulse control (double-pulse control) at T within the duration of 4.0 after the last subpulse as with Fig. 4(a). For example, we obtain $<W(T)>_{\max}^{(5)}=0.64$, 0.58, 0.53, 0.50 and 0.47 at $T=2$ K, 3 K, 5 K, 7 K and 10 K, respectively, which lead to $s(T=2,3,5,7\text{ K})=1.20$ and $s(T=10\text{ K})=1.19$. These values of $s(T)$ suggest the advantage of the use of the control pulse composed of more than two subpulses over that of the double pulse at least in the low-temperature region.

To reduce the number of subpulses, we first evaluate the contribution of each subpulse in Fig. 3. We find that the first *Y* subpulse makes the least contribution to the 3D alignment. We thus remove the subpulse and impose a large penalty on that temporal region through the function, $\gamma(t)$, which prevents the optimization algorithm from reproducing the removed *Y* subpulse. We then re-optimize the remaining *X*, *Y*, *X,* and *Y* subpulses to adjust their fluence and temporal peak positions. Note that the re-optimization does not generate any extra subpulses. After the re-optimization, we replace the four subpulses in the new optimal pulse with the four Gaussian subpulses in the same manner as that in Fig. 5(a). The result is shown in Fig. 5(b) and will be referred to as a quadruple-pulse control scheme. We see from the inset in Fig. 5(b) that the quadruple-pulse control scheme leads to the averaged degree of alignment of 0.72, which is near the value achieved by the quintuple-pulse control scheme. Similarly, we can derive the triple-pulse control scheme as shown in Fig. 5(c), in which the new control pulse consists of the *X*, *X,* and *Y* subpulses. Note that the control pulses in Figs. 3 and 5(a)–(c) have the same total fluence of 1.1 J/cm^2 within two significant digits, which is smaller than that used in the double-pulse control (1.3 J/cm^2) in Fig. 4(a).

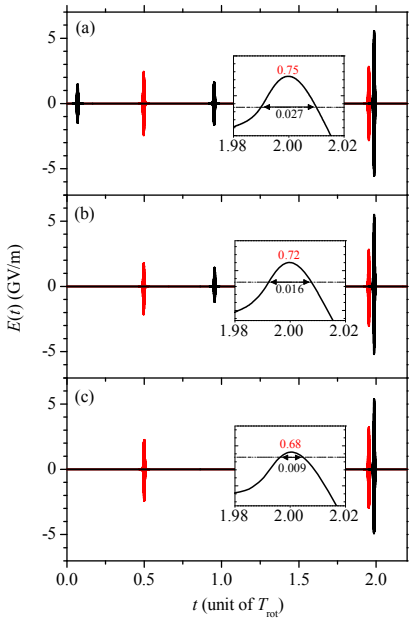

Figure 5

Optimally designed Gaussian subpulses in the (a) quintuple-pulse control, (b) quadruple-pulse control, and (c) triple-pulse control schemes. Each inset shows a magnified view of the time evolution of the averaged degree of alignment in which the maximum value is given. The horizontal dashed lines specify 0.67, which is the maximum averaged degree of alignment achieved by a pair of optimal double Gaussian subpulses with the total fluence of 1.3 J/cm^2. The period (units of T_{rot}) during which the averaged degree of alignment is larger than 0.67 is also shown in each inset.

We see from the insets in Fig. 5 that the maximum values of the averaged degrees of alignment monotonically increase as the number of subpulses is increased. Even the triple-pulse control with the total fluence of 1.1 J/cm^2 leads to better 3D alignment than the double-pulse control with the total fluence of 1.3 J/cm^2. Although the extent of the increase is not significant, the triple-pulse control can keep the highly aligned state for 236 fs, as indicated by the horizontal dashed line in the inset. (The dashed line shows 0.67, i.e., the maximum averaged degree of alignment achieved by the double-pulse control.) That period will be

sufficiently long to induce, e.g., electronic dynamics in the molecule-fixed frame. The introduction of more subpulses leads to a longer period, such as 707 fs [Fig. 5(a)] and 419 fs [Fig. 5(b)], during which the highly aligned state is maintained. As the control pulse is composed of simple subpulses, which is experimentally feasible, we confirm the superiority of the control pulse composed of more than two linearly polarized subpulses to achieve high degrees of 3D alignment.

IV. Summary

We have applied nonlinear optimal control simulation to the 3D alignment of SO_2, in which the time-dependent polarization vectors of a non-resonant laser pulse are also fully optimized. In Fig. 2, we optimized non-resonant laser pulses to find the optimal polarization conditions, the suitable set of target axes, the suitable final time, t_f, etc. The optimized pulses are always composed of combinations of mutually orthogonal, linearly polarized subpulses. We also found that the target axes associated with the two largest polarizability components, i.e., the *a*- and *b*-axes, lead to the largest averaged degree of alignment and the optimal pulse with the simplest structure although the differences in value among the optimized degrees of alignment are small. In Fig. 3, choosing the *a*- and *b*-axes as the target, we optimized the non-resonant laser pulse with final time $t_f = 2.0$ (in units of rotational period) to discuss the control mechanisms in detail. Our discussion is based on the time derivatives of the expectation values of the squares of the direction cosines and that of the free rotation Hamiltonian, H_0, which are connected to each other through Eq. (13). We have emphasized the important and special role of the last subpulse that accounts for more than 60% of the total fluence. The last subpulse simultaneously aligns the *b*- and *c*-axes, which are associated with

the two smallest polarizability components, while minimizing undesirable torque on the *a*-axis. The other subpulses appear at the right timings predicted by Eq. (13) to effectively induce the rotational excitation through the largest polarizability component. We have also shown that all the subpulses in the optimal pulse can be replaced with simple subpulses, such as Gaussian subpulses, provided that they impulsively excite the rotational wave packet. Because the double-pulse control leads to the saturation of the degrees of alignment as a function of total fluence [Fig. 4(b)], we conclude the superiority of the use of more than two linearly polarized subpulses to achieve high degrees of 3D alignment (Fig. 5).

Acknowledgements

One of the authors (YO) acknowledges support from a Grant-in-Aid for Scientific Research (C) (15K05373) and partly from the Joint Usage/Research Program on Zero-Emission Energy Research, Institute of Advanced Energy, Kyoto University (ZE30B-16). This work was also partly supported by a Grant-in-Aid for JSPS Fellows (17J02010). N.T. acknowledges support from the Israel Science Foundation (1094/16) and the German-Israeli Foundation for Scientific Research and Development (GIF) for the main part of the work at Department of Chemical Physics, Weizmann Institute of Science. N.T. further acknowledges the Chemical Sciences, Geosciences, and Biosciences Division, Office of Basic Energy Sciences, Office of Science, US Department of Energy under Award No. DE-FG02-86ER13491 for support during the preparation of the manuscript.

References

[1] R. N. Zare, "*Angular Momentum*" (Wiley, New York, 1988).

[2] D. Herschbach, *Eur. Phys. J. D* **38**, 3 (2006).

[3] B. Friedrich and D. Herschbach, *Phys. Rev. Lett*. **74**, 4623 (1995).

[4] P. M. Felker, *J. Phys. Chem*. **96**, 7844 (1992).

[5] H. Stapelfeldt and T. Sideman, *Rev. Mod. Phys*. **75**, 543 (2003).

[6] T. Seideman and E. Hamilton, *Adv. At. Mol., Opt. Phys*. **52**, 289 (2006).

[7] Y. Ohtsuki, M. Yoshida, K. Nakashima, K. Arai, and K. Nakajima, *Adv. Multi-photon Processes and Spectroscopy*, **13**, 55 (2016).

[8] J. G. Underwood, B. J. Sussman, and A. Stolow, *Phys. Rev. Lett*. **94**, 143002 (2005).

[9] K. F. Lee, D. M. Villeneuve, P. B. Corkum, A. Stolow, and J. G. Underwood, *Phys. Rev. Lett*. **97**, 173001 (2006).

[10] S. S. Viftrup, V. Kumarappan, S. Trippel, H. Stapelfeldt, E. Hamilton, and T. Seideman, *Phys. Rev. Lett*. **99**, 143602 (2007).

[11] S. S. Viftrup, V. Kumarappan, L. Holmegaard, C. Z. Bisgaard, H. Stapelfeldt, M. Artamonov, E. Hamilton, and T. Seideman, *Phys. Rev. A* **79**, 023404 (2009).

[12] M. Artamonov and T. Seideman, *Phys. Rev. A* **82**, 023413 (2010).

[13] D. Takei, J. H. Mun, S. Minemoto, and H. Sakai, *Phys. Rev. A* **94**, 013401 (2016).

[14] A. Rouzée, S. Guérin, O. Faucher, and B. Lavorel, *Phys. Rev. A* **77**, 043412 (2008).

[15] S. Pabst and R. Santra, *Phys. Rev. A* **81**, 065401 (2010).

[16] X. Ren, V. Makhija, V. Kumarappan, *Phys. Rev. Lett*. **112**, 173602 (2014).

[17] Y. Ohtsuki and K. Nakagami, *Phys. Rev. A* **77**, 033414 (2008).

[18] H. Abe and Y. Ohtsuki, *Chem. Phys*. **400**, 13 (2012).

[19] C. Brif, R. Chakrabarti, and H. Rabitz, *New. J. Phys*. **12**, 075008 (2010).

[20] Y. Ohtsuki, W. Zhu, and H. Rabitz, *J. Chem. Phys*. **110**, 9825 (1999).

[21] H. Abe and Y. Ohtsuki, *Phys. Rev. A* **83**, 053410 (2011).

[22] M. Yoshida and Y. Ohtsuki, *Phys. Rev. A* **90**, 013415 (2014).

[23] H. M. Frey, P. Beaud, T. Gerber, B. Mischler, P. P. Radi, and A. P. Tzannis, *J. Raman Spectrosc*. **31**, 71 (2000).

[24] D. Xenides and G. Maroulis, *Chem. Phys. Lett*. **319**, 618 (2000).

[25] The usefulness of Eq. (13) can be even more clearly illustrated if we consider one-dimensional alignment control of symmetric top or linear molecules by using a linearly polarized laser pulse.